

Growth, Electrical and Magnetic Investigations of Manganese Oxide Thin Films



A thesis submitted towards the partial fulfillment
of BS-MS Dual Degree Programme

By

Rushikesh Prakash Magdum

(20151176)

Under the guidance of

Prof. Satishchandra B. Ogale

Emeritus Professor and Raja Ramanna Fellow

Department of Physics

Submitted to

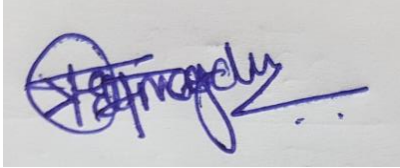
Department of Physics

Indian Institute of Science Education and Research (IISER)

Pune

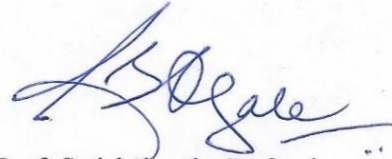
Certificate

This is to certify that this dissertation entitled “Growth, Electrical and Magnetic Investigations of Manganese Oxide Thin Films” towards the partial fulfillment of the BS-MS dual degree program at the Indian Institute of Science Education and Research, Pune represents study/work carried out by **Rushikesh Prakash Magdum** under the supervision of **Prof. Satishchandra B Ogale**, Emeritus Professor and Raja Ramanna Fellow, Department of Physics during the academic year 2019-2020.



Rushikesh Prakash Magdum

Registration Number: 20151176



Prof. Satishchandra B. Ogale

Professor

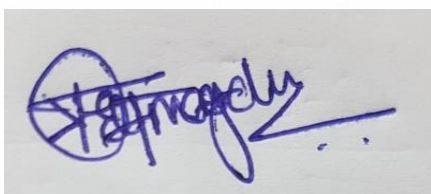
Committee:

Prof. Satishchandra B. Ogale (Supervisor)

Dr. Mukul Kabir (Expert)

Declaration

I hereby declare that the matter embodied in the report entitled “Growth, Electrical and Magnetic Investigations of Manganese Oxide Thin Films” are the results of the work carried out by me at the Department of Physics, IISER Pune, under the supervision of Prof. Satishchandra B. Ogale and the same has not been submitted elsewhere for any other degree.



Rushikesh Prakash Magdum

Registration Number: 20151176



Prof. Satishchandra B. Ogale

Professor

Acknowledgments

I would like to express my sincere gratitude and respect to my thesis supervisor Prof. Satishchandra B. Ogale, for his constant inspiration and contribution throughout my research period. I am indebted to excellent mentorship from Dr. Abhijit Biswas and Mr. Rajesh Mandal for my research work. Their regular inputs and suggestion helped my projects move forward. I am grateful to my amazing lab members for giving continuous support and creating a lively environment throughout this project.

I am thankful to Dr. Ram Janay Choudhary, UGC-DAE-CSR, Indore for magnetic, dielectric, and magnetodielectric measurement. I would also like to thank Mr. Suresh Bharadwaj and Ms. Sophia Sahoo for carrying out the dielectric and magnetodielectric measurements. I thank Mr. Umashankar Rajput for the AFM measurement. I am also grateful to the Department of Science and Technology (DST), for the INSPIRE fellowship program and administrative and non-administrative staff at IISER Pune for their constant provision.

Finally, I am very thankful to my whole family for their constant love, care, and support. I am also indebted to my beloved friends for their continuous help and support.

Contents

1. Introduction:	1
1.1 Manganese oxides	1
1.2 Dielectric	1
1.3 Magnetic	3
1.4 Magnetodielectric	4
1.5 Applications of magnetodielectric materials	5
1.6 Spinel Structure	6
2. Experimental Section	9
2.1 Making a target	9
2.2 Pulsed Laser Deposition	9
2.3 Analysis Techniques	12
2.3.1 X-ray Diffraction	12
2.3.2 X-ray Photoelectron Spectroscopy	14
2.3.3 Atomic Force Microscopy	14
2.3.4 Raman Spectroscopy	15
2.3.5 SQUID-Magnetometer	16
2.3.6 Dielectric and Magnetodielectric Measurement	18
3. Results and Discussion:	19
3.1 θ - 2θ X-ray Diffraction	19
3.2 X-ray Photoelectron Spectroscopy	20
3.3 Atomic Force Microscopy	21
3.4 Raman Spectrum	22
3.5 Magnetization	23
3.6 Dielectric and Magnetodielectric data	24
4. Conclusion and Future Studies	27
5. Bibliography	28

List of Figures

Figure 1: Spinel structure of Mn ₃ O ₄ showing tetrahedrons and octahedrons	7
Figure 2: PXRD data of Bragg's plane of α -Mn ₂ O ₃ powder used for making target	9
Figure 3: Schematic of Pulsed Laser Deposition	10
Figure 4: All the Euler axes in HRXRD and Bragg's law illustration	12
Figure 5: Basic design of the AFM	15
Figure 6: Energy level diagram for Raman Scattering and Rayleigh Scattering	16
Figure 7: XRD data of Pulsed Laser deposited thinfilm	19
Figure 8: X-ray Photoelectron spectrum of deposited thinfilm	20
Figure 9: Shows the surface morphology of the film obtained via AFM	21
Figure 10: Raman Spectrum of deposited thinfilm	22
Figure 11: SQUID-Magnetometer data	23
Figure 12: Dielectric and Magneto-dielectric measurement data and xrd of device	25

List of Tables

Table 1: Comparing d-spacing and strain for (111) and (202) orientation of Mn ₃ O ₄	20
Table 2: Character table for D _{4h} point group	22

Abbreviations

PLD	Pulsed Laser deposition
XRD	X-ray Diffraction
PXRD	Powder X-ray Diffraction
AFM	Atomic force Microscopy
XPS	X-ray Photoelectron Spectroscopy
CFSE	Crystal Field Stabalization Energy
SQUID	Superconducting Quantum Interference Device
VSM	Vibrating Sample Magnetometer

Abstract

In the last few decades, research in oxides has grown up tremendously due to the observation of emergent multifunctional phenomena, e.g., ferromagnetism, ferroelectricity, multiferroicity, high-temperature superconductivity, metal-insulator transitions, giant magnetoresistance and more recently the topological Hall Effect. These phenomena arise because of the interplay between the fundamental degrees of freedoms, which are charge, lattice, spin, and orbital. Mostly, oxide-based materials are found to be less susceptible to degradation in air, giving an ideal platform for next-generation device applications.

In my final year project, by using Pulsed Laser Deposition (PLD), I have grown Mn_3O_4 thinfilms. This oxide shows huge promises for tunable magnetic and dielectric properties. The x-ray diffraction has been demonstrated that we have oriented growth along the $[h0h]$ directions. The XPS confirms that our thinfilm is Mn_3O_4 , removing doubt of the presence isostructural gamma phase of Mn_2O_3 . We have a ferrimagnetic transition at the 42K, and magnetodielectric data also shows this transition along with transitions at 40K and 33K in compliance with reported data. However, we observe the coercivity of 8600Oe at 5K, which is almost three times the reported data.

Chapter 1

Introduction

1.1 Manganese Oxides

For the device applications, the material must have stability at room temperature. This stability comes naturally to the metal oxides because of oxygen presence. Also, oxides show many novel properties such as superconductivity, ferromagnetic, ferroelectric, multiferroic, high spin polarization, metal-insulator transition, magnetostriction, magnetoresistance, and many more^[1]. As manganese shows the valence state from +2 to +7, this gives a range of manganese oxides, which are MnO, Mn₃O₄, Mn₂O₃, and MnO₂ in the increasing order of their Mn:O ratio. These oxides also show many phases that give rich physics for studying the materials.

By taking advantage of the epitaxial growth of oxide thin films, one can not only grow varieties of metal oxides but also can reduce the dimension of the material down to the monolayer limit to obtain unforeseen phenomena, which are absent in bulk. Dimensionality reduction is found to be one of the classic routes to achieve quantum emergent phenomena in physical systems (due to the size effects, edge states, charge and spin redistribution, strain onto film), giving rise to the quantum confinement effect.

Using pulsed laser deposition, we made thinfilms of a manganese oxide. We chose to work on Mn₃O₄ to explore its magnetodielectric coupling and optimize its growth to incorporate this oxide for heterostructured multiferroic thinfilm study. To study magnetoelectric coupling it is necessary to understand the dielectric and magnetic phenomena.

1.2 DIELECTRIC:

For material to be a good dielectric, it has to be insulators because if the material is metal, then upon application of an electric field, there will be a flow of charges which will not create dipoles. So, for insulators, when we apply the external electric field, there is a displacement of the negative cloud center from a positively charged cloud center. This separation of charges occurs as the direction of Coulomb force depends on the polarity of charge, and the Coulomb force is given by the following formula:

$$\mathbf{f}=\mathbf{qE}$$

where f is a force acting on the charge q and E is the electric field strength at that charge position which is given by

$$E = \frac{Q}{4\pi\epsilon r^2}$$

where Q is the charge, which is producing electric field, r is the distance between the source charge and the point where we are finding the electric field, and ϵ is the permittivity of the medium in which we have an electric field. There are four ways by which materials get polarized:

1. **Electronic Polarization:**

For neutral atom, it has the same number of electrons and protons, and the center of these charges lies at the same place, which leads to no net dipole moment. But when we apply the external electric field, the Coulomb force acting in the opposite direction for the positive and negative charges which result in a neutral atom but with non-zero net electric dipole moment. This displacement of charges is even true for a charged ion. As it is just a displacement of charges from their equilibrium position, it is regarded as an elastic displacement, and it is almost independent of the temperature.

2. **Atomic or ionic Polarization:**

In this type of polarization, there is a displacement of the atoms or ions when we apply the external electric field. This is also referred to as vibrational polarization, as it distorts the lattice structure. Like electronic polarization, this is also elastic displacement, and it has a slight dependence on the temperature.

3. **Orientalional Polarization:**

This type of polarization is possible for material which possesses permanent dipole moment. So, when we apply the external electric field to minimize the energy, dipole moments align anti-parallel to the direction of the external field. As we know that lattice vibrations depend on the temperature, this polarization also depends on the temperature. Also, there is a loss of energy as heat due to inertia experienced by the reorientation of dipoles.

4. **Space Charge Polarization:**

The charge carriers present in the material are responsible for space charge polarization. This charge carriers from the contact get trapped inside the defects present in the materials which creates polarization.

The time required for the above polarization to take place varies in the following order: Electronic < Atomic < Orientational < Space-Charge.

1.3 Magnetism:

In given material, we have magnetic properties because of the orbital and the spin angular momentum of its constituting ions. However, we can have different magnetic properties for different phases of the chemical compound, such as α - Mn_2O_3 is antiferromagnetic, and γ - Mn_2O_3 is ferromagnetic^[2,3]. This happens as a different structure gives rise to various interactions of the atomic/ionic magnetic moments.

The following Hamiltonian gives the interactions between the neighbouring spins^[4]:

$$H = -\frac{1}{2} \sum_{i,j} J_{ij} \mathbf{S}_i \cdot \mathbf{S}_j + \sum_i g \mu_B \mathbf{B} \cdot \mathbf{S}_i - k \sum_i (\mathbf{S}_i^{\text{easy}})^2$$

where \mathbf{S}_i and \mathbf{S}_j represent the spins on the neighboring atom or ion i and j respectively, and J_{ij} is exchange constant. If we have $J_{ij} > 0$, then we have ferromagnetic interaction leading to an alignment of the neighboring spins, whereas $J_{ij} < 0$ gives antiferromagnetic interaction, which has neighboring spins aligned antiparallely. The second term is Zeeman energy, which considers perturbation of the system when the magnetic field is applied. The magnetic moment of electron points opposite to the direction of its spin as

$$\boldsymbol{\mu} = g \frac{q}{2m} \mathbf{L}$$

where $\boldsymbol{\mu}$ is magnetic moment generated by the charge of q with mass m having angular momentum \mathbf{L} . The Lande g -factor depends on spin and orbital angular momentum and their coupling. The last term is known as the anisotropic term. In a given crystal structure, we have a specific direction along which it is energetically favorable to have a magnetic moment. This direction is known as an easy axis. Along this direction, we have a smaller number of magnetic ions, which result in the saturation of magnetization in a low applied field. This term includes S_i^{easy} , which is a projection of angular momentum along the anisotropic direction, and k is anisotropic constant.

The interactions between spins give rise to magnetization, which is a magnetic moment per unit volume. As energy density due to the magnetic field is proportional to the B^2 and magnetic dipole-dipole interaction is given by:

$$H = -\frac{\mu_0}{4\pi|r|^3}[3(\mathbf{m}_1 \cdot \hat{\mathbf{r}})(\mathbf{m}_2 \cdot \hat{\mathbf{r}}) - \mathbf{m}_1 \cdot \mathbf{m}_2] + \mu_0 \frac{2}{3} \mathbf{m}_1 \cdot \mathbf{m}_2 \delta(\mathbf{r})$$

where \mathbf{m}_1 and \mathbf{m}_2 are magnetic dipoles which separated by vector \mathbf{r} , as energy decreases when we have magnetic moments anti-aligned, this leads to the formation of domains inside the material. So, these domains have net magnetization, which points in a different direction, and resultant is zero.

The application of the magnetic field enforces these random magnetic moments to point along the applied magnetic field direction as it decreases energy due to Zeeman energy. This can be done either by rotating spins or moving the domain wall so that their magnetic moments point along the field.

There is a cost for the formation of domain walls, and its thickness depends on the exchange constant and the anisotropy constant. If we have anisotropy constant larger than exchange constant, we will have thinner domain walls; otherwise, we will have thicker domain walls which can vary coercivity if we have smaller crystallite size.

1.4 Magnetodielectric Coupling:

In magnetoelectric material, we have a coupling of magnetic and electric properties present in the material. This given by following the free energy equation^[5,6,7]:

$$F(\mathbf{E}, \mathbf{H}) = F_0 + P_i E_i - M_i H_i - \frac{1}{2} \epsilon_0 \epsilon_{ij} E_i E_j - \frac{1}{2} \mu_0 \mu_{ij} H_i H_j - \alpha_{ij} E_i H_j - \frac{\beta_{ijk}}{2} E_i H_j H_k - \frac{\gamma_{ijk}}{2} H_i E_i E_k - \dots$$

where ϵ_{ij} and μ_{ij} are relative permittivity and permeability of the medium, respectively. α , β , γ are magnetoelectric coefficients. The i , j , and k represent components of the \mathbf{E} and \mathbf{H} . In magnetodielectric material, we have magnetic ordering coupled with the dielectric property of a material. So, our free energy equation becomes:

$$F(\mathbf{E}, \mathbf{H}) = -M_i H_i - \frac{1}{2} \epsilon_0 \epsilon_{ij} E_i E_j - \frac{1}{2} \mu_0 \mu_{ij} H_i H_j - \alpha_{ij} E_i H_j - \frac{\beta_{ijk}}{2} E_i H_j H_k - \frac{\gamma_{ijk}}{2} H_i E_i E_k - \dots$$

The term $-\alpha_{ij} E_i H_j$ gives linear magnetoelectric coupling. We have the following mechanisms by which we can see this magnetoelectric coupling:

1. Superexchange Striction

The superexchange interaction is one of the many exchange interactions which facilitates the communication between different spins^[8]. This is mainly observed where we have magnetic ions (M) with the same oxidation states, and there is a non-magnetic ion (N) between these magnetic ions. The non-magnetic ion acts as a mediator between these magnetic ions to enable spin orientation across the material, which gives long range order. We get an insulator with antiferromagnetic interaction when we have an overlap between the magnetic and non-magnetic ion orbitals because of the lowering of kinetic energy. However, we have ferromagnetic interaction when we have no overlap. As overlap between these orbitals is subjected to bond length and bond angle, the ion displacement because of an electric field can modify magnetic interaction between these ions.

2. Single-Ion Anisotropy

As stated earlier, magnetic anisotropy arises as the particular direction is preferred for the orientation of magnetic moments over others. So, when we apply the external electric field, there is a change of the crystal structure environment surrounding these magnetic ions, which leads to a change in magnetic anisotropy direction, and so does the net magnetic moment. This is how spin, orbital, lattice, and charge degrees of freedom get coupled in this type of magnetoelectric material.

3. Strain Driven Magnetoelectric Heterostructured Effect

This type of magnetoelectric coupling is observed in artificially synthesized heterostructures of magnetic and electric materials^[9]. This coupling is communicated via the interface between these materials. If we have a heterostructure of ferromagnetic and ferroelectric material when we apply the electric field, it will generate polarization in the ferroelectric material. As ferroelectric materials are also piezoelectric material, the electric field will induce mechanical strain on it. This strain will produce strain in the ferromagnetic material, which will result in a change in its magnetic interactions and net magnetic moments.

1.5 Applications of Magnetoelectric Material:

- It can be used to probe the magnetic and structural properties using electric field studies and vice versa.
- Store the data using magnetic field and reading it using electric field response to save energy^[10].
- These materials can be used for data storage, sensors and transducers.

From above it is clear that structure is very important aspects which decides various interactions. Here, we discuss the spinel structure of Mn_3O_4 .

1.6 Spinel Structure:

Spinel is a class of structure with formula AB_2X_4 , where A and B are different cations, and X is an anion. Mostly, A has an oxidation state of +2, and B has oxidation states of +3. They have either cubic or tetragonal crystal structure. Anions are arranged in the cubic closed packing, which gives rise to tetrahedral sites and octahedral sites. A and B cation arrange themselves according to their oxidation state, splitting field of the ligand, which happens to have high crystal field stabilization energy. For normal spinel, A occupies the tetrahedral site, and B holds the octahedral site. But for inverse spinel, one B occupies the tetrahedral place, and another B with A occupies the octahedral site.

Crystal Field Stabilization Energy:

Before the approach of the ligands, central metal ion has a spherical field, which gives degenerate d-orbitals, i.e., all d-orbitals are at the same energy level, which is known as barycentre. Crystal field comes into the picture when six ligands approach a central metal ion that has degenerate orbitals, which becomes non-degenerate to lower the electronic repulsion between the central metal atom and the ligand. In the octahedral crystal field, i.e., ligands approach central metal atom along the axes of the octahedral structure, so we have maximum repulsion along the axes of an octahedron. This leads to stabilization (gets lowered in energy) of the d-orbitals, which are in-between the axes and destabilization (gets higher in energy) of the d-orbitals, which are along the axes as shown in the figure. This leads to the splitting of d-orbitals into two groups known as, e_g and t_{2g} , which contains $d_{(x^2-y^2)}$, $d_{(z^2)}$ and d_{xy} , d_{yz} , d_{xz} , respectively. Then filling of these d-orbitals depends on Hund's rule and strength of the ligand's electric field.

Hund's Rule:

Hund's rule of maximum multiplicity states that the filling of orbitals is such that it tries to maximize the total spin to have lower energy. As each d-orbital can have a maximum of two electrons, filling of electrons is such that each d-orbital is filled with only one electron, and their spin is parallel to each other.

Spectrochemical series is a series that gives the electric field strength of the ligand. Stronger the field more will be the splitting of the d-orbitals. If we have strong field ligands in

an octahedral field and four d-electron to fill, then the fourth electron will pair up an electron in lower energy d-orbital rather than going to a higher energy d-orbital. This will, in turn, change the crystal field stabilization energy.

Similarly, in the tetrahedral crystal field, four ligands approach central metal atom from in-between the axes. So, d-orbitals of the central metal atom are stabilized, which are along the axes and destabilized, which are in-between the axes. For the same ligands, a central metal atom, and distance between them, we will have smaller splitting between d-orbitals in the tetrahedral field compared to an octahedral field, which is given by relation $\Delta_T = -4/9\Delta_O$. This is also a reason why octahedral complexes are stable compared to tetrahedral complexes.

If a cation has higher CFSE in the octahedral crystal field than another cation, then it will prefer octahedral site, and other cation will be in tetrahedral sites. To illustrate this, consider Mn_3O_4 in which we have one Mn^{+2} and two Mn^{+3} . Since Mn has atomic number $Z=25$ with an electronic configuration of $[Ar] 3d^5 4s^2$. So, electronic configuration for Mn^{+2} is $[Ar] 3d^5$ and for Mn^{+3} it is $[Ar] 3d^4$. As oxygen is strong field ligand, we get $(t_{2g})^3(e_g)^2$ for Mn^{+2} and $(t_{2g})^3(e_g)^1$ for Mn^{+3} for the octahedral field, which gives higher CFSE for Mn^{+3} . For every system, it is important to have lower energy, so we get Mn^{+2} in the tetrahedral site and Mn^{+3} in the octahedral site giving us a normal spinel structure.

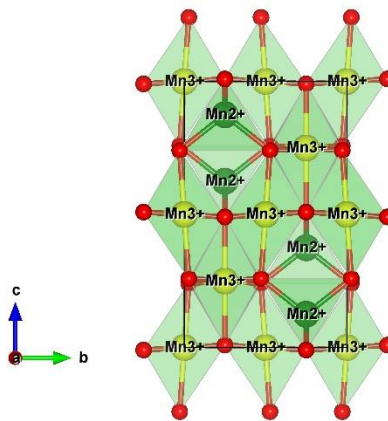


Figure 1: Spinel structure of Mn_3O_4 showing tetrahedrons and octahedrons.

The Jahn Teller distortion is a distortion of crystal structure to remove the degeneracy of the crystal field. This distortion is prominent when we have degeneracy in destabilized d-orbitals, i.e., e_g orbitals in the octahedral crystal field because we have maximum repulsion of the ligand and central metal atom for these orbitals. This distortion removes the crystal field degeneracy and also lowers the overall energy and symmetry of the system. Since we have

$(t_{2g})^3(e_g)^1$ for Mn^{+3} for the octahedral field, which gives two degenerate states: $(t_{2g})^3(dz^2)^1$ or $(t_{2g})^3(dx^2-y^2)^1$, this degeneracy leads to Jahn-Teller distortion at 1440K^[11] where crystal structure of Mn_3O_4 gets converted to tetragonal spinel from cubic spinel.

In spinel structure, we have four octahedral sites, and eight tetrahedral sites and two octahedra are occupied by B cation, and A cation occupies one of the eight tetrahedral sites. Figure 1 shows the unit cell, which has four formula units of Mn_3O_4 .

Chapter 2

Experimental Section

2.1 Making a Target

To grow thinfilm using Pulsed Laser Deposition (PLD), it required to have a target to be homogenous, strong, and polished. So, we used α - Mn_2O_3 powder from Alfa Aesar, which has 98% purity. I also performed powder x-ray diffraction (PXRD) on this powder to confirm its phase. PXRD data shown in Figure 2 indeed corroborate phase of the Mn_2O_3 to be alpha with a cubic unit cell as earlier reported^[2].

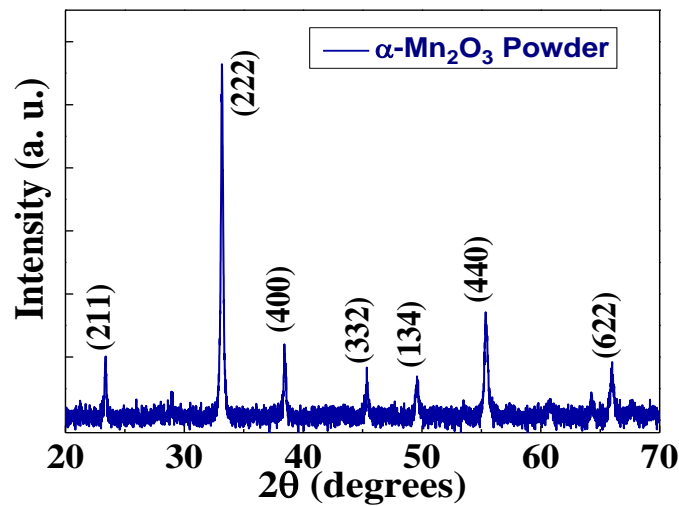


Figure 2: PXRD data of Bragg's plane of α - Mn_2O_3 powder used for making target.

After verifying the phase of powder, I grounded the powder using mortar and pestle for an hour to ensure its homogeneity further and to make it usable in KBr press for making a pellet for a target. Then using a 20mm die set, we made a pellet from the finely grounded powder. By using a furnace with oxygen supply, we sintered our pellet for 24 hours at 1200 °C. Ramping and cooling of temperature took 10 hours each.

We used silver paste and glued the pellet to the target holder and placed it in the oven for 10 minutes for adhesion. Then we mounted the target inside the PLD chamber.

2.2 Pulsed Laser Deposition (PLD):

PLD is a physical vapor deposition technique. This is a widely used technique to grow high quality, defect-free thinfilm for materials and device applications^[12]. In this method, we use Excimer laser with short-pulsed duration and very high coherence length. The laser we

used was a KrF excimer laser with a wavelength of 248nm. We can control the energy density of laser (energy of laser per unit area) by controlling source voltage as we can vary the spot size of the laser beam^[13]. It is important to note that for a fixed amount of voltage, we can get different energy density because it also depends on the amount of KrF gas in the laser cavity. We can also use quartz glass to minimize the energy density as per our requirement. Then we have a lens to focus the laser beam on the target. When the laser hits the target because of its high energy density and coherence, the material of the target gets ablated, and plasma is formed. However, we kept the target rotating at 15Hz to avoid the drilling of the target.

In the chamber, as shown in the figure 3, we can introduce gas to influence the path of the plasma plume, change the kinetic energy of plasma constituents and to incorporate gas constituents into the film to be deposited^[14]. Depending on the pressure of gas, plasma plume's shape gets altered, and this also changes the rate of deposition if we keep all other variables constant.

We mount the substrate on the substrate holder using silver paint epoxy. Cleaning of the substrate should be done before installing it on the substrate holder to avoid any foreign contamination in the film. After making the chamber clean, we have to use a rotary pump and turbo molecular pump to create a vacuum inside the chamber to avoid any contamination further. We have to raise substrate temperature to a suitable temperature to facilitate the movement of the plasma constituent on the substrate surface to form a crystal structure. While doing deposition, we have to change the pressure inside the chamber using gas inlet as per the requirement of our film growth. This substrate temperature also affects the kinetics of plasma in the chamber^[15]. Kinetics of plasma reaching the substrate, which is set parallel to the target, also depends on the target to substrate distance, the mass of constituents of plasma and laser energy density.

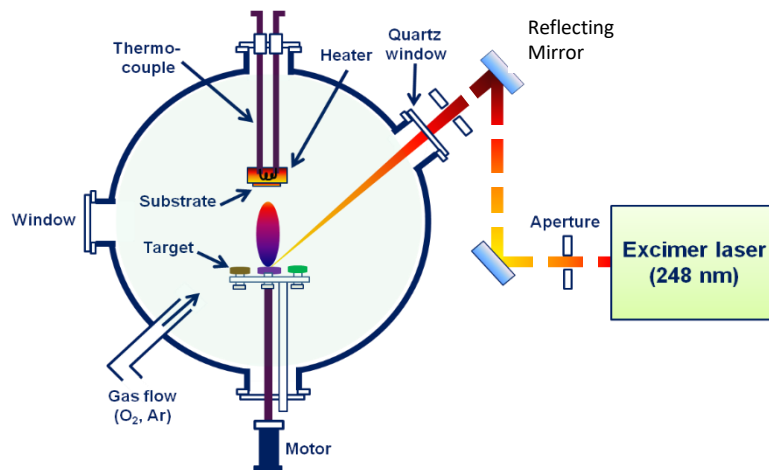


Figure 3: Schematic of Pulsed Laser deposition chamber.

For film deposition, it is essential to choose a proper substrate. The substrate provides the framework of arrangement for plasma constituents falling on it. Epitaxial growth of film happens when lattice parameters of the film and the substrate at the interface match. So. It is crucial to choose a substrate with proper lattice parameters and its orientation towards plasma plume for good nucleated growth of the film. As temperature plays a vital role in film growth, it becomes mandatory to look into the thermal properties such as thermal expansion, the thermal stability of both film and substrate to be in close vicinity; otherwise, it might damage the film and the substrate after the cooling^[16]. We should also take care that substrate and film should not react with each other, and temperature should be maintained such that it avoids diffusion of plasma inside it. Also, if the lattice mismatch between the film and the substrate is not too much and can facilitate epitaxial growth, this can give us a film of the same in-plane lattice constant as that of the substrate and different out-of-plane lattice parameter of the film from its bulk material. This can lead to new properties such as centrosymmetric (bulk) to non-centrosymmetric(film), which will give us net polarization in the film, which is absent in bulk.

Strain in the film with respect to bulk is give by:

$$\text{Strain} = (a-a_0)/a_0$$

where a is lattice parameter of thinfilm and a_0 is the same corresponding lattice parameter of the bulk single crystal of the same material.

The parameters discussed above with different combination can give us three distinct modes of growth:

1. Franck-van der Merwe Growth (layer by layer):

In this mode of growth, interactions between adsorbate-surface and adsorbate-adsorbate are balanced, which gives ideal thin film growth.

2. Stranski-Krastanov Growth (joint islands):

Adsorbate-surface interaction is stronger than adsorbate-adsorbate interaction favoring the growth of islands that are close to each other.

3. Volmer-Weber Growth (isolated islands):

In this case, adsorbate-adsorbate interaction is stronger than that of the adsorbate-surface interaction, which leads to the formation of islands on the surface, which are separated from each other.

2.3 Analysis techniques:

2.3.1 X-ray Diffraction

X-ray diffraction is one of the methods to probe the structural details of the materials. It can be performed for polycrystalline as well as a crystalline sample.

- Bragg's law

In crystalline material, we have a periodic arrangement of the atom, which looks like the periodic arrangement of the planes. In a family of planes, we have planes that are parallel to each other, and interplanar distance between the two consecutive planes is constant. This law states that for a given wavelength and given interplanar distance d , which is characteristic of a family of planes, these planes behave like a mirror for a particular value of incident angle of x-ray. This is shown in the following figure 4(b) and 4(c).

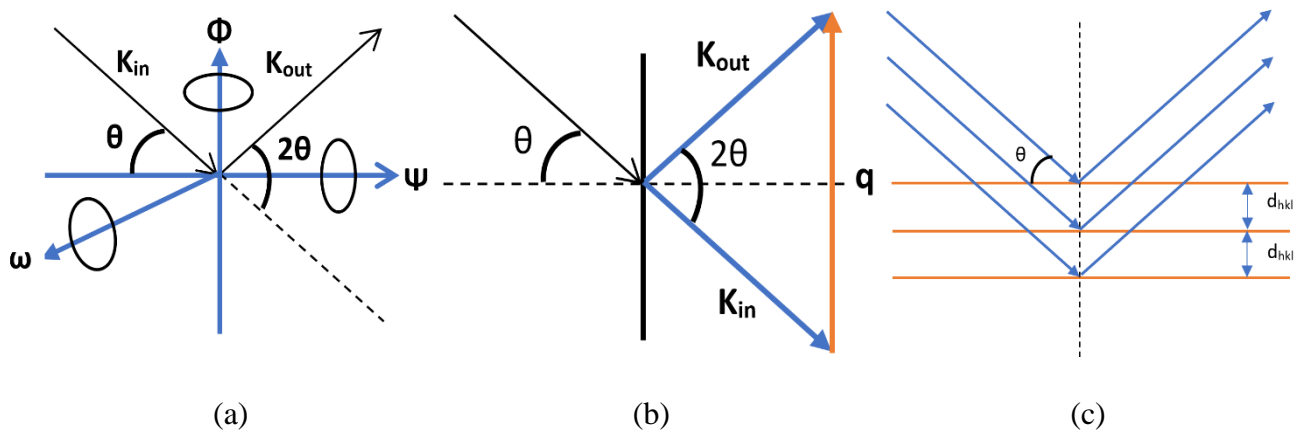


Figure 4 : (a) shows all the axes used for high-resolution XRD. (b) illustrates the scattering of incident X-ray and (c) shows the same for the family of Bragg's plane.

XRD diffraction can be performed in different modes for the crystalline sample as listed below:

2.3.1.1 Powder X-ray Diffraction (θ - 2θ scan):

Powder x-ray diffraction is a θ - 2θ scan. In this mode, x-ray coming from the Cu K- α source make an angle of θ with the sample, and the detector used for measuring diffraction intensity makes an angle of 2θ with the source. During θ -scan for different planes in the sample, the source and detector both move to maintain θ - 2θ relation. According to Bragg's law, we get constructive interference for a particular value of θ relating to d_{hkl} value for (hkl) planes present in the sample. Using the values of d_{hkl} and its intensity, we construct the crystal structure. For

single crystalline material, we get the only family of planes that are parallel to each other. So, we have to rotate our crystal along the Euler axes shown in figure (a) to get other families of planes, and from them, we construct our crystal structure.

2.3.1.2 High-Resolution X-ray Diffraction:

a) 2θ - Ω Scan

In this mode of the scan, the length of the scattering vector \mathbf{q} is varied while keeping its direction constant. With the help of a symmetric scan, one can identify phases incorporated in the film, presence of distortion, and coherence length of the crystallite along the direction of the scattering vector, which is perpendicular to the film surface.

b) Ω Scan

During Ω -scan, the length of the scattering vector is kept constant, and it sweeps a circular path around the origin of reciprocal lattice space. We can also make the rocking motion of the film to get Ω -scan, so it is also known as the rocking curve. This gives us information about the lateral coherence length of the film, tilt of the crystallites in the film.

c) Reciprocal Space Map

This is Ω -scan coupled with 2θ - Ω Scan. This is a 2D scan, so we see the elliptical feature instead of the broadening of a peak, which is observed in Ω -scan and 2θ - Ω Scan. From this, we can calculate the strain present in the film, the lattice parameters of the film, and whether our film is epitaxial or not.

d) Φ Scan

It is performed for a fixed value of Ω and θ corresponding to the plane, which we want to probe. The sample is rotated around Φ -axis for 360° , which also rotates reciprocal space around the origin, and as the length of the scattering vector is fixed, we get symmetry of the plane. If the plane which is under examination is six-fold symmetric, we get six peaks in the interval of 60° . For epitaxial growth of the thin film on the substrate, substrate and film peaks appear at the same value as the Φ .

2.3.2 X-ray Photoelectron Spectroscopy

X-ray photoelectron is another novel X-ray based technique that is used to know the chemical composition of the material. In this method, X-ray is produced from Al K- α , which has the energy of 1486.7eV. X-ray source, sample, and electron detector are kept in the ultra-high vacuum chamber. Monochromatic x-ray is incident on the surface of the material, which interacts with the electrons in the material. According to the photoelectric effect, photoelectron, which is an ejected electron, has kinetic energy, which depends on the energy of the incident electron and binding energy of the electron, which is emitted. In XPS, we also have to take into account the work function of material and the detector, which is denoted by ϕ . By using the following relation, we get binding energy of the photoelectron

$$E_{B.E.} = E_{\text{Photon}} - (\text{K.E. of electron} + \phi)$$

As monochromatic x-ray has some amount of energy width and there are also inelastic collisions inside material, which gives us broadening around the $E_{B.E.}$ of the photoelectron. We can have a collision of the ejected photoelectron with other species in the chamber before reaching the detector. This may result in higher and lower K.E. of photoelectron, which will lead to higher or lower $E_{B.E.}$. So, it is very critical to have an ultra-high vacuum to ensure the correctness of the binding energy.

As we know that binding energy of the electron depends on the quantum numbers of the electron, charge state of the ion containing the electron, and electronic environment of the ion. If our material contains ions of the same element with different charge states, then we will have an overlap of the binding energy. As the detector records the kinetic energy of the photoelectron and also counts the number associated with it, we can fit the different curves inside the raw XPS data peak and find out the charge state of ions along with their ratio. We used XPSPEAK41 software to deconvolute obtained spectra.

2.3.3 Atomic Force Microscopy

Atomic force microscopy is one of the scanning probe microscopy technique, which is used for imaging. The basic design for AFM imaging is shown in figure 5. This technique is based on the force between the material surface under the study and the tip of the cantilever. As the tip of the cantilever approaches the material surface, it experiences forces like van der Waals force because of the material surface, and it gets attracted or repelled from the surface depending on the distance between the surface and the tip. We also have laser and photodetector, which records the deflection in the cantilever. This deflection gives the

information about the cantilever tip distance and along with the spatial XY-plane coordinate for which imaging is being performed. This is used to get a 3D topological image by performing a raster scan. This scan can be achieved in two modes:

1. Contact Mode:

In this mode, the cantilever is moved on the surface, and the deflection of the tip is recorded. As a material surface, in general, is non-uniform, we get different deviation which can help us to map the surface of the material. Since material surface can have sudden jumps, this can cause damage to the tip of the cantilever.

2. Tapping Mode:

We oscillate the tip of the cantilever and record the deflection of the cantilever for tapping mode AFM imaging. Using the deflection, we adjust the material surface or cantilever along the normal direction to the material surface. This deflection is used by a feedback mechanism, which then adjusts the tip of the cantilever so that force between the surface and the tip is maintained at the fixed value. This mode ensures the less damage of the tip, which is vital as the resolution of the image depends on the tip size.

Using this data and pseudocolor, which corresponds to a particular depth, we get the surface image. This 3D image also gives information about the roughness of the film.

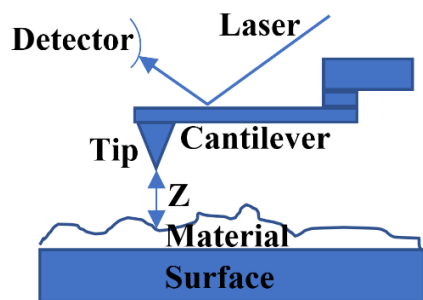


Figure 5 : Basic design of the AFM. Z indicates the tip and material surface.

2.3.4 Raman Spectroscopy

Raman spectroscopy is based on Raman scattering, which is the inelastic scattering of electromagnetic waves. This is a non-resonant spectroscopic technique. When electromagnetic waves get incident on the material because of the electric field in the electromagnetic wave, its

polarization changes. This leads to material going to the excited virtual state and returns to the different rovibronic (rotation-vibrational-electronic) state. This is different from IR spectroscopy in which material absorbs the incident laser beam, and it goes to different vibrational levels. Also, for IR spectroscopy selection rules dictates the change of the polarization while in Raman, it is necessary to have change in polarizability between final and initial state. For centrosymmetric molecules, the mutual exclusion principle states that IR active modes are Raman inactive and vice versa. But for other molecules, Raman active mode has very less IR absorption intensity and vice versa.

In Raman spectroscopy, we measure a shift in the energy as given below as it is inelastic scattering. This shift corresponds to a vibrational energy level, which gives information about the structural details such as length and geometry of the bonding.

$$\Delta\lambda = \left(\frac{1}{\lambda_i} - \frac{1}{\lambda_s} \right)$$

where λ_i is the wavelength of the incident laser, and λ_s is the wavelength of the scattered laser. Scattering phenomena can be elastic as well as inelastic. Elastic scattering ($\lambda_i = \lambda_s$), which is also known as Rayleigh scattering, has very high intensity compared to inelastic scattering, i.e., Raman scattering. Raman scattering can have a Stokes shift in which scattered laser has lower energy than incident laser and vice versa for an anti-Stokes shift. Figure 6 compares various scattering phenomena.

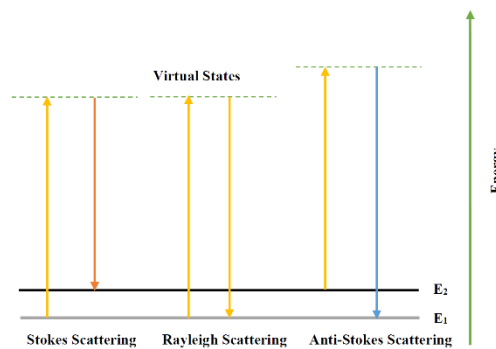


Figure 6 : Energy level diagram for Raman Scattering and Rayleigh Scattering

Since the intensity of scattering depends on the population of the initial state, which results in Raman scattering with Stokes shift to have higher intensity compared to one with the anti-Stokes shift. This happens because as energy increases, we get a lower population from Maxwell-Boltzmann distribution.

2.3.5 SQUID-Magnetometer

SQUID:

The superconducting quantum interference device (SQUID) is a device which consists of Josephson junction, two superconductors separated by an electrical insulating layer. This junction helps us to measure the slight change in the magnetic field, which is necessary for accurate measurement of magnetization for spintronics application.

VSM-Magnetometer:

Faraday's law states that change in the magnetic field will induce the electromotive force (e.m.f.). We apply the magnetic field, which is along the length of the superconducting pickup coil, and also vibrates our sample along the direction of the applied field. The superconducting coil is always inside the helium bath and thermally isolated from the sample, and it is arranged in such a way that other external magnetic fields like earth's magnetic field can be ignored. The external magnetic field induces magnetization in our sample, and its magnetization depends on the magnetic field strength and magnetic properties of the material. The vibrating motion of the magnetized sample induces emf, which is proportional to the total moments in the sample and produces a current in the pickup coil, which then generates the magnetic field which acts on the SQUID. As SQUID is very sensitive to the magnetic field, it generates a current which is then amplified by the external circuit. This current is then used to get the total moments present in the sample.

For a given material, there is magnetic anisotropy depending on its crystal structure and magnetic atom's arrangement and their interaction. This provides an easy axis, which is the direction in the crystal along which we have saturation magnetization with a low external applied magnetic field. During zero-field cooling, our moments get aligned along the easy axis below the magnetic transition temperature. While warming, we apply the magnetic field at 5K, which tries to reorient the magnetization along its direction. So, magnetization developed is very small.

But when we apply the magnetic field while cooling the sample in field cooled measurement, magnetic moments get frozen in the applied field direction. So, when we start recording the data while warming, we have enough magnetization developed inside the sample, which in comparison with the zero-field cooling data can give bifurcation at the magnetic transition temperature. So, this data is useful to get the magnetic transition temperature. But here we have to keep the magnetic field low because otherwise high magnetic field perturbs the system, which makes it challenging to observe systems inherent nature. All magnetic measurements were performed using 7-Tesla SQUID-Vibrating Sample Magnetometer (SVSM), Quantum Design Inc., USA.

2.3.6 Dielectric and Magnetodielectric Measurement

We performed the dielectric measurement using the Alpha-A High-Performance Frequency Analyzer from NOVO-Control. The dielectric probe for this measurement was designed for bulk analysis where dielectric measurement is performed in parallel plate capacitor geometry. So, for thinfilm, we have to grow our film such that we can fit our thinfilm in that configuration. This controller measures the impedance of the thinfilm in that configuration, and using the relation between the impedance, frequency, and capacitance; we get the value of the capacitance. First, we calibrate our controller using the standard BaTiO₃, which is a ferroelectric ceramic metal oxide. Using the relation between the capacitance, area of the parallel plate, and distance between the parallel plate, we obtain dielectric constant of the material. We get real and imaginary values of impedance, which then results in real and imaginary values of the capacitance and so the dielectric constant. The real part of the dielectric constant signifies the ability of the material to store the energy in it when an electric field is applied, and the imaginary part signifies the loss of energy while storing the energy in the material.

Magneto-dielectric measurement gives direct evidence for magneto-dielectric coupling in the material. In this measurement, we do the dielectric analysis with a magnetic field applied parallel to the electric field. We performed magnetodielectric measurement using a 9T superconducting-magnet Integra System from Oxford Instruments.

Chapter 3

RESULTS AND DISCUSSION

3.1 θ -2 θ X-ray Diffraction Result

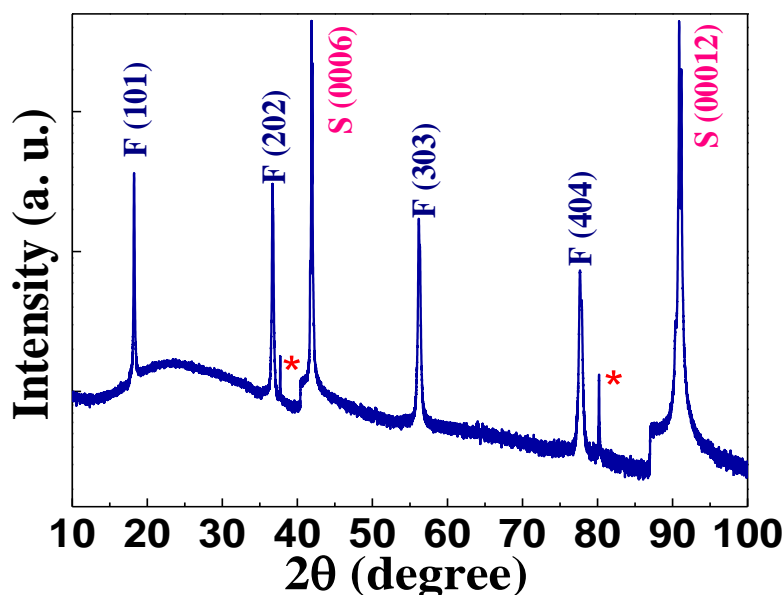


Figure 7 : X-ray diffraction of 100 nm Mn_3O_4 thin film grown on $c\text{-Al}_2\text{O}_3$ (0001) substrate. Asterisk (*) is from the substrate. F corresponds to film peaks whereas S denotes substrate peaks.

After growing film, we performed a θ -2 θ scan on film to see the structure of the film and if we require further optimization of PLD parameters for proper growth of the film. The 2 θ scan of the film shown in the figure 7, which shows that the structure of the material is in correspondence with the $\gamma\text{-Mn}_2\text{O}_3$ and Mn_3O_4 . Also, we got oriented growth along the [h0h] direction. As $\gamma\text{-Mn}_2\text{O}_3$ and Mn_3O_4 have the same space group which is $I4_1/amd$ with lattice parameters $a=b=5.8 \text{ \AA}$, $c=9.4 \text{ \AA}$, and $\alpha=\beta=\gamma=90^\circ$. Since we only got a parallel family of planes in the tetragonal structure, this resulted in the relation between a and c as $a^2c^2=24(a^2+c^2)$ obtained using (202) plane's 2 θ value and Bragg's law. After putting value of $a=5.8 \text{ \AA}$, we got $c=9.4 \text{ \AA}$ which is in agreement with the literature values^[17].

From the XRD data, we are observing the direction of growth on the c -plane of the hexagonal Al_2O_3 substrate to be [h0h]. For ideal thinfilm growth, it is expected from the growing film to adopt the symmetry of the substrate. As the substrate has six-fold symmetry,

we can expect our film growth to have six-fold or three-fold symmetry. Since we are growing tetragonal spinel, it has a three-fold axis along the [hhh] direction. So, we should be observing (111), (222), (333), and so on for Mn₃O₄ growth. But we see growth along the [h0h] direction, which do not have a three-fold or six-fold symmetry. As lattice matching is also an essential parameter for film growth, we calculated the strain for films with [h0h] and [hhh] direction growth using the following formula:

$$\text{Strain} = \frac{d(f) - d(s)}{d(s)} \times 100\%$$

where d(f) is d-spacing of the film along the film growth direction and d(s) is d-spacing of the substrate along the film growth direction. As its turnout, the strain for [202] direction growth is 14.79%, and for [111] directional growth, it is 74.41%. As the system is always preferred to be in an unstrained condition, it automatically prefers the growth along the [h0h] direction. Bogle et al. also reported this as the reason behind their growth on Mn₃O₄ on STO(111) substrate^[18]. This substrate also has the three-fold axis symmetry along the direction of growth. However, it is essential to find out why [h0h] direction was preferred over other directions.

	Mn ₃ O ₄ d-spacing	Al ₂ O ₃ d-spacing	Strain
Mn ₃ O ₄ (111)/Al ₂ O ₃ (0006)	3.75902	2.15	74.41%
Mn ₃ O ₄ (202)/Al ₂ O ₃ (0006)	2.468	2.15	14.79%

Table 1: Comparing d-spacing and strain for (111) and (202) orientation of Mn₃O₄.

Since we are not able to corroborate whether our material is γ -Mn₂O₃ or Mn₃O₄, we performed further characterizations discussed below.

3.2 X-ray Photoelectron Spectra

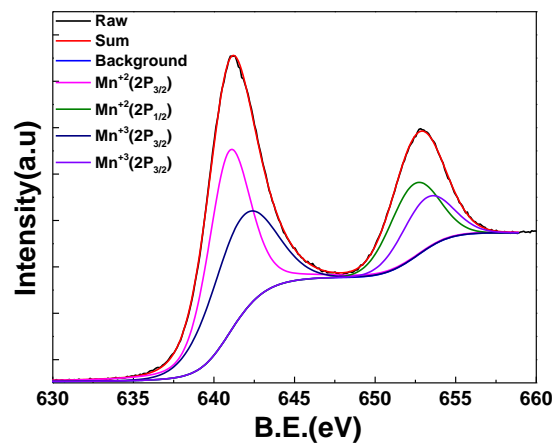


Figure 8 : X-ray photoelectron spectrum shows the Mn⁺³ and Mn⁺² oxidation state.

We did x-ray photoelectron spectroscopy to confirm the chemical nature of the film. The raw data obtained was fitted using the XPSPEAK41 software using a Shirley background. We also carbon corrected the data using C 1s peak at a binding energy of 284.6eV. The optimized fitted data is shown in figure 2. The Mn $2P_{3/2}$ and $2P_{1/2}$ have a binding energy of 641.22eV and 652.82eV, respectively. This gives a spin-orbit splitting of 11.6eV, which is in close agreement with reported data for Mn_3O_4 ^[19]. The energy positions obtained for $2P_{3/2}$ of Mn^{+2} and Mn^{+3} are 641.12eV and 642.42, while for $2P_{1/2}$ of Mn^{+2} and Mn^{+3} are 652.72eV and 653.63eV, respectively which confirms our material as Mn_3O_4 .

3.3 Atomic Force Microscopy:

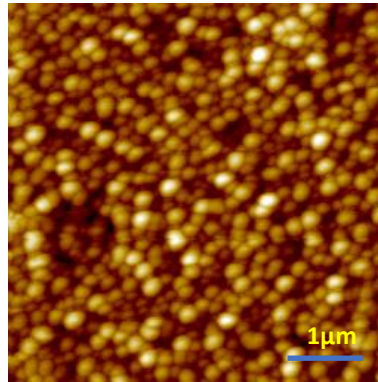


Figure 9 : Shows the surface morphology of the film obtained via atomic force microscopy.

As one can use AFM to measure the roughness of the material, we were interested in measuring the thickness of the sample. So, we covered some part of the substrate to avoid deposition and did the film growth on the uncovered part. This film is then used to measure the thickness of the film as we get step height at the interface of the covered and exposed part of the film. The thickness of the film turned out to be 100nm for 10000 shots of the deposition. We kept this thickness fixed for all other deposition.

We scanned the $5\mu m \times 5\mu m$ area on the film, which is shown in figure 9. We got the RMS roughness of 5nm, and the average grain diameter is 200nm. As our deposition rate is 5Hz, which is giving less time for the redistribution of the plasma content on the substrate. Also, as our deposition temperature is $700^\circ C$, but we are cooling the temperature just after the deposition. These two factors might be responsible for this 5nm roughness observed. If we keep the temperature at deposition temperature for some time, we might get low roughness.

As it has been observed that if we maintain our substrate at deposition temperature for some time, the roughness of the film decreases. This happens because temperature provides energy for the redistribution of surface species. However, we also have to take into account the

interaction between the adsorbate-adsorbate and the adsorbate-substrate; if we have stronger adsorbate-adsorbate interaction, we might get high roughness. This happens because we get isolated islands and roughness will be in the vicinity of the thickness of the film.

3.4 Raman Spectrum

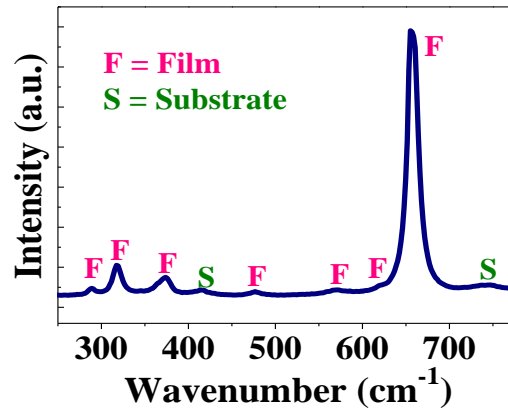


Figure 10 : Raman Spectra shows the peaks correspond to the spinel structure. F: Film and S: Substrate

D_{4h}	E	$2C_4(z)$	C_2	$2C_2'$	$2C_2''$	i	$2S_4$	σ_h	$2\sigma_v$	$2\sigma_d$	Linear, rotations	Quadratic
A_{1g}	1	1	1	1	1	1	1	1	1	1		x^2+y^2, z^2
A_{2g}	1	1	1	-1	-1	1	1	1	-1	-1	R_z	
B_{1g}	1	-1	1	1	-1	1	-1	1	1	-1		x^2-y^2
B_{2g}	1	-1	1	-1	1	1	-1	1	-1	1		xy
E_g	2	0	-2	0	0	2	0	-2	0	0	(R_x, R_y)	(xz, yz)
A_{1u}	1	1	1	1	1	-1	-1	-1	-1	-1		
A_{2u}	1	1	1	-1	-1	-1	-1	-1	1	1	z	
B_{1u}	1	-1	1	1	-1	-1	1	-1	-1	1		
B_{2u}	1	-1	1	-1	1	-1	1	-1	1	-1		
E_u	2	0	-2	0	0	-2	0	2	0	0	(x, y)	

Table 2: Character table for D_{4h} point group.

Raman spectra for our film is shown in the figure 10. As space group of Mn_3O_4 is $I4_1/amd$, which corresponds to the D_{4h} point group. Table 2 shows the character table for this point group. As for Raman excitation of the material, it is required to have a change in polarizability, which needs have a quadratic function for the irreducible representation. So, we have four Raman active modes correspond to the A_{1g} , B_{1g} , B_{2g} , and E_g modes.

The peak at 655cm^{-1} is associated with the MnO_6 octahedra vibrations present in the spinel structure, which is also observed in the $\alpha\text{-Mn}_2\text{O}_3$ and RMnO_3 , which has perovskite structure. The peaks at the 374cm^{-1} and the 317cm^{-1} are assigned to the bending of O-Mn-O and Mn-O-Mn, respectively^[20]. Our data is in close resemblance with the data reported by T. Larbi et al. confirming good growth of Mn_3O_4 .

3.5 Magnetization Result:

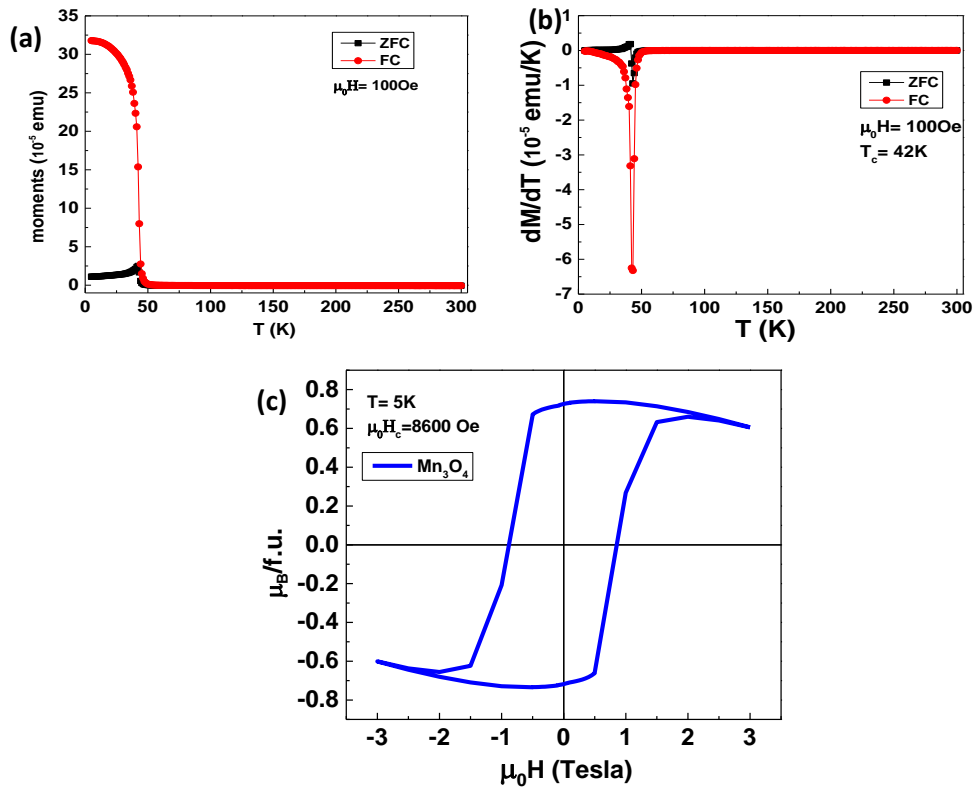


Figure 11 : (a) and (b) shows moments and its first derivative versus temperature, respectively. Field cooled (FC) and zero-field cooled (ZFC) magnetic measurements show the magnetic ordering below 43K. (c) shows moments as a function of applied field at 5K.

To investigate the magnetic transition in our thinfilm, we carried out magnetization as a function of temperature. In this measurement, we did zero-field cooling (zfc) and field cooling (fc) measurement. For zero-field cooling, we cooled our sample in SQUID-magnetometer to 5K and then applied the magnetic field of 100Oe and recorded the magnetization while warming the sample to 300K. Similarly, for field cooling measurement, we followed the same protocol with cooling the material to 5K in the presence of 100Oe magnetic field instead of zero magnetic field. This data is shown in the above figure 11(a).

As from the figure, we can see the bifurcation of zfc and fc curve at 43K. This transition temperature is coincident with a ferrimagnetic transition temperature of Mn_3O_4 , which is also 43K (ref) and near the ferromagnetic transition temperature of γ - Mn_2O_3 , which is 39K^[31]. Below we have shown the $\frac{dM}{dT}$ as a function of temperature, which also shows transition temperature to be 43K as shown in figure 11(b). After confirming the magnetic transition temperature, we varied the external magnetic field and observed the magnetization at 5K, which is below the magnetic transition temperature. This data is shown in figure 11(c). We have a hysteresis loop

with the coercivity of 8680 Oe and a saturation magnetization of $0.72 \mu_B$ per formula unit. The saturation magnetization reported for Mn_3O_4 is $1.85 \mu_B$ per formula unit and has a coercivity of 2650 Oe at 4.2K^[21]. There is no data available for saturation magnetization of γ - Mn_2O_3 . But as reported by S. H. Kim et al., it has a coercivity of almost 8000 Oe^[3].

Our sample consists of thinfilm material with the sapphire substrate. So, magnetic data has the contribution of both material as well as the substrate. We know that sapphire is diamagnetic, and our thinfilm material is ferromagnetic, so we are not able to get Curie-Weiss plot to know whether our material has ferromagnetic or antiferromagnetic interaction. But it is reported that Mn_3O_4 is ferrimagnetic, where Mn^{+3} moments align anti-parallel to Mn^{+2} moments^[22]. Since γ - Mn_2O_3 does not have Mn^{+2} as it has vacant tetrahedral sites, it has ferromagnetic interaction. As the thickness of the film is 100nm and that of the substrate is 1mm, we might be getting lower saturation magnetization.

The large discrepancy observed for the coercivity of Mn_3O_4 can be explained by a single domain particle nature of thinfilm. From the AFM morphology images, we have granular growth. Our grains are crystallites, and the size of the grains is around 200nm from AFM and thickness is 100nm; this might be resulting single domain nature of the grains giving observed coercivity. We need further carry out the measurement to investigate low saturation magnetization observed. However, it can also possibly due to oxygen vacancies present in the material. These vacancies can also explain high coercivity because of domain wall pinning^[23].

3.6 Dielectric and Magnetodielectric Measurement:

To see if our material possesses magnetodielectric coupling, we performed dielectric and magnetodielectric measurements. Since it required to have parallel plate geometry to perform a dielectric measurement, we deposited 20nm of $SrRuO_3$, a conducting oxide, on c - Al_2O_3 and then deposited 100nm of the Mn_3O_4 on it. XRD of this device is shown in figure 12(a). As discussed earlier, we see the growth of $SrRuO_3$ along (111) as it has cubic symmetry. We can see that here also we have oriented growth of the Mn_3O_4 and $SrRuO_3$.

We performed the dielectric measurement with the applied voltage of 1V. We recorded the capacitance by varying the temperature from 300K to 6K. As we were getting contact problems, we did all our measurements between 6K to 60K with the measurement at each 0.25K increment. We recorded the capacitance data for frequency of 316kHz. From data, we can infer the transition at 43K and 39K. The transition at 43K is the magnetic phase transition.

As we increase magnetic field which is parallel to the direction of the electric field in parallel plate capacitor of our material, we can see that dielectric constant also increases for the magnetic field of 0.1 Tesla, and it shows an increase in dielectric constant for temperature above 12.5K and decreases in ϵ below 12.5K for the magnetic field of 0.5 Tesla. These observations are confirmed in the following figure where we calculated magnetodielectric (MD) change in percentage using the following formula

$$\text{MD}\% = \frac{\epsilon(H) - \epsilon(0T)}{\epsilon(0T)} * 100\%$$

where $\epsilon(H)$ is dielectric constant with the applied field, and $\epsilon(0T)$ is dielectric constant at zero magnetic fields at the same temperature. The highest value of MD% observed is 0.08% at 33K which is also in close agreement with the reported data at 30K by TACKETT et al.^[23]

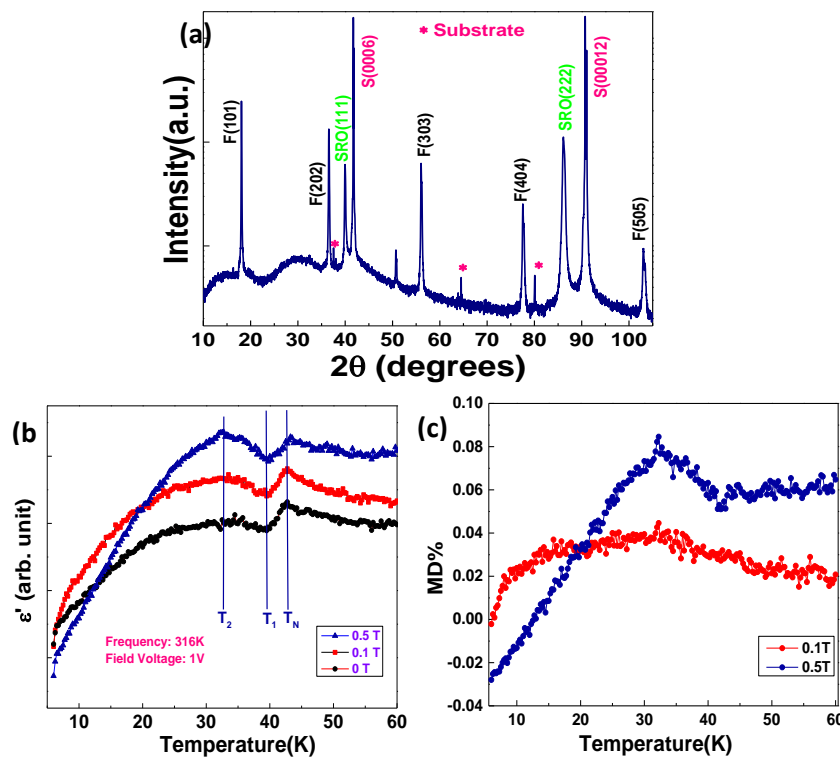


Figure 12 : (a)XRD data showing peaks for SrRuO₃, F: Mn₃O₄, and S: Al₂O₃. (b) The relative permittivity of the film with different magnetic fields showing the various transitions. (c) MD% variation with respect to the temperature recorded at 0.1T and 0.5T.

It is observed that as we increase the applied magnetic field, we see transition at the 32.75K. This transition is reported to correspond with the unit cell doubling along the a-axis of the tetragonal spinel structure of the Mn₃O₄^[21].

Tacket et al. reported that magnetic phase ordering starts at 43K^[22]. As Mn₃O₄ is ferrimagnetic, we have spins of Mn⁺³ from octahedral sites to order ferromagnetically with each other similar as that of Mn⁺² from tetrahedral sites, and Mn⁺² spins arrange antiferromagnetically with Mn⁺³ spins. Below 39K we have incommensurate phase where we have chemical unit cell not in proportion with the magnetic unit cell. However, we get commensurate phase below 33K which has chemical unit cell doubled with respect magnetic unit cell. As dielectric constant is subjected to atomic arrangement, we see prominence of this transitions in magnetodielectric data.

Chapter 4

Conclusion and Future Studies

We synthesized the oriented crystalline thinfilm of Mn_3O_4 with (h0h) orientation. Because of low dimensions and growth parameters, we achieved the high coercivity essential for device application. The chemical nature of the thin film is indeed Mn_3O_4 as from the x-ray photoelectron spectroscopy. The Raman data shows all reported Raman modes of Mn_3O_4 . The magnetic transition observed at 43K is in agreement with earlier reported data. However, we need to investigate the reason behind the low saturation magnetization. The magnetodielectric effect was studied with the various magnetic field, and it indeed shows the charge, spin, and lattice coupling. The dielectric data with the magnetic field also shows that our material is Mn_3O_4 as it shows all three transitions observed at $T_N=43\text{K}$, $T_1=39\text{K}$, and $T_2=33\text{K}$. We saw the enhancement of dielectric constant at transition temperature of $T_2=33\text{K}$ as we increase the magnetic field.

In future studies, we plan to explore the growth of manganese oxides at different oxygen partial pressure, substrate temperature, and using the various substrate. I will grow Mn_3O_4 on various substrate, and using thinfilm x-ray diffraction, and various structural techniques will find the reason behind the [h0h] oriented growth. Also, using density functional theory, we will find about this oriented growth. I will also try to synthesize $\gamma\text{-Mn}_2\text{O}_3$ and compare it with Mn_3O_4 . Since, it is apparent from the magnetodielectric data that we have very weak coupling, we will couple the magnetic property of Mn_3O_4 with the other ferroelectric oxide to study how interface mediates the magnetic and electric coupling. We will also study magnetic, electrical and magnetoelectric measurements at various fields and frequencies. I will reduce the thickness further to see if we can see any quantum confinement and dimensional effect.

Bibliography

- [1] Izyumskaya, N., Alivov, Y., & Morkoç, H., Oxides, Oxides, and More Oxides: High- κ Oxides, Ferroelectrics, Ferromagnetics, and Multiferroics, *Critical Reviews in Solid State and Materials Sciences*, 34(3-4), 89–179.
- [2] Mohit Chandra, Satish Yadav, R. J. Choudhary, R. Rawat, A. K. Sinha, Marie-Bernadette Lepetit, and Kiran Singh, Multiferroicity and magnetoelastic coupling in α -Mn₂O₃: A binary perovskite, *PHYSICAL REVIEW B*, 98, 104427 (2018).
- [3] S. H. Kim, B. J. Choi and G. H. Lee, Ferrimagnetism in γ -Manganese Sesquioxide (γ -Mn₂O₃) Nanoparticles, *Journal of the Korean Physical Society*, Vol. 46, No. 4, April 2005, pp. 941-944.
- [4] The Oxford Solid State Basics Book by Steven H. Simon.
- [5] Martin, L. W.; Ramesh, R., Multiferroic and Magnetoelectric Heterostructures., *Acta Mater.*, 2012, 60 (6–7), 2449–2470.
- [6] L. D. Landau and E. M. Lifshitz, *Electrodynamics of continuous media* (Fizmatgiz, Moscow, 1959).
- [7] Manfred Fiebig, Revival of the magnetoelectric effect, *J. Phys. D: Appl. Phys.*, 38 (2005) R123–R152.
- [8] T. Kimura, T. Goto, H. Shintani, K. Ishizaka, T. Arima & Y. Tokura, Magnetic control of ferroelectric Polarization, *Nature*, volume 426, pages 55–58 (2003).
- [9] Khomskii, D. Classifying Multiferroics: Mechanisms and Effects. Physics (College. Park. Md). 2009, 2, 20
- [10] N. A. Spaldin and R. Ramesh Nature Materials VOL 204 18 MARCH 2019 203–212
- [11] Changsoo Kim, Euna Jo, Byeongki Kang, Sangil Kwon, and Soonchil Lee Giant magnetic anisotropy in Mn₃O₄ investigated by ⁵⁵Mn²⁺ and ⁵⁵Mn³⁺ NMR PHYSICAL REVIEW B 86, 224420 (2012)
- [12] T. Miller, Laser Ablation. Principles and Applications ~Springer, Berlin, 1994
- [13] T. Ohnishi, H. Koinuma, M. Lippmaa, Pulsed laser deposition of oxide thin films, *Applied Surface Science*, 252 (2006) 2466–2471
- [14] A. Sambri, S. Amoruso, X. Wang, F. Miletto Granozio, and R. Bruzzese, Plume propagation dynamics of complex oxides in oxygen, *J. Appl. Phys.*, 104, 053304, 2008
- [15] A. Sambri, M. Radovic', X. Wang, S. Amoruso, F. Miletto Granozio, R. Bruzzese, *Applied Surface Science* 254 (2007) 790–793.

- [16] Julia M. Phillips, Substrate selection for high-temperature superconducting thin films, *J. Appl. Phys.*, 79 (4), 15 February 1996.
- [17] Jarosch, D Crystal structure refinement and reflectance measurements of hausmannite, Mn_3O_4 , *Mineralogy and Petrology* (1987), 37, 15-23.
- [18] K. A. Bogle, V. Anbusathaiah, M. Arredondo, J. Lin, Y. Chu, C. O'Neill, J. M. Gregg, M. R. Castell, and V. Nagarajan, Synthesis of Epitaxial Metal Oxide Nanocrystals via a Phase Separation Approach, *ACS Nano*, 2010, 4, 9, 5139-5146.
- [19] V.C. Bose, V. Biju, *Physica E*, 66, (2015), 24–32.
- [20] T. Larbi, K. Doll, T. Manoubi, Density functional theory study of ferromagnetically and ferrimagnetically ordered spinel oxide Mn_3O_4 . A quantum mechanical simulation of their IR and Raman spectra, *Journal of Alloys and Compounds*, Volume 688, Part A, 15 December 2016, Pages 692-69.
- [21] K. Dwight and N. Menyuk, Magnetic Properties of Mn_3O_4 and the Canted Spin Problem, *PHYSICAL REVIEW*, VOLUME 119, Number 5.
- [22] R. Tackett and G. Lawes, Magnetodielectric coupling in Mn_3O_4 , *PHYSICAL REVIEW B* 6, 024409, 2007.
- [23] Lorenzo Bigiani et al. High Magnetic Coercivity in Nanostructured Mn_3O_4 Thin Films Obtained by Chemical Vapor Deposition *ACS Appl. Nano Mater.* 2019, 2, 3, 1704-1712.